3D pore cloud-informed deep learning framework for multiscale structure–energy absorption correlation in porous sandwich materials

Zhang, Jiaxiu; Zhao, Wei; Chen, Ran; Nan, Liangliang; Chen, Wenhao; Wei, Mingqiang

DOI
10.1016/j.compstruct.2025.119910

Publication date
2026

Document Version
Final published version

Published in
Composite Structures

Composite Structures 378 (2026) 119910

Contents lists available at ScienceDirect

Composite Structures

journal homepage: www.elsevier.com/locate/compstruct

3D pore cloud-informed deep learning framework for multiscale structure–energy absorption correlation in porous sandwich materials

Jiaxiu Zhang [a], Wei Zhao [a,*], Ran Chen [a], Liangliang Nan [b], Wenhao Chen [c], Mingqiang Wei [a,*]

[a] Nanjing University of Aeronautics and Astronautics, Nanjing, 211106, China
[b] Delft University of Technology, Delft, 2628BL, Netherlands
[c] Southeast University, Nanjing, 211189, China

ARTICLE INFO

Dataset link: https://crescentrosexx.github.io/pore-net/

Keywords:
3D pore cloud
Aluminum foam sandwich
Energy absorption
Structural characterization
Deep learning

ABSTRACT

Porous sandwich structures, particularly aluminum foam sandwiches (AFS), are widely used in lightweight and impact-resistant applications, yet their mechanical performance remains difficult to predict due to irregular and multiscale pore morphologies. Traditional constitutive models and current deep learning methods fall short in capturing the complex structure–property relationships of those materials. Accordingly, this work proposes a three-dimensional (3D) pore cloud representation learning method tailored for energy absorption prediction. A novel digital descriptor, termed the pore cloud, is constructed from 3D scans of real AFS cores to preserve detailed pore-level geometric and topological information. A comprehensive structure–property dataset is subsequently generated by integrating these pore cloud features with energy absorption data obtained through finite element analysis (FEA). Furthermore, this work develops PoreNet, a point cloud-based deep learning architecture that learns the direct mapping from mesoscale pore morphology to macroscopic mechanical response. The experimental results demonstrate that PoreNet achieves a high prediction accuracy of 95.12%, robust generalization across variable porosities, and fast convergence within 30 min on a consumer-grade Graphics Processing Unit (GPU). It outperforms both traditional analytical models and baseline neural networks. In addition, this study demonstrates the effectiveness of pore-level geometric learning in structure–property modeling and offers a scalable, data-driven framework for the design and optimization of advanced porous sandwich composites. The dataset and the proposed algorithm are publicly available at https://crescentrosexx.github.io/pore-net/.

1. Introduction

In the era of lightweight and high-performance engineering, structural composite materials have become indispensable in modern industrial systems [1]. Among them, porous sandwich structures that comprise stiff face sheets and a lightweight core stand out due to their superior strength–weight ratios, energy dissipation capabilities, and impact resistance [2]. These advantages have driven widespread application in safety-critical fields such as automation, automotive industry, aerospace, industrial protection [3]. Aluminum Foam Sandwich (AFS), which incorporates an aluminum foam core with a unique porous architecture, exhibits outstanding mechanical behavior, including high specific energy absorption, thermal and acoustic insulation, and mechanical damping [4]. As their integration into crashworthy and high-impact structural components becomes increasingly widespread, accurately predicting their mechanical response becomes critical to guide material design and ensure the reliability of the application [5,6]. However, accurate prediction of the mechanical behavior of the AFS remains a formidable challenge, primarily due to the complex topology, irregularity, and highly stochastic nature of the foam core mesostructure. This internal architecture comprises randomly distributed interconnected pores and struts whose geometric and topological variability profoundly influences macroscopic performance [7]. Local defects such as cell wall rupture, pore clustering, or asymmetric connectivity further complicate the response of the system under load [8]. As a result, establishing robust structure–property relationships remains a fundamental and unresolved challenge in the mechanics of heterogeneous porous media.

From a theoretical perspective, this bottleneck is due to the lack of a unified framework capable of capturing multiscale interactions, particularly the way in which mesoscopic pore morphology governs large-scale mechanical behaviors such as energy absorption, failure initiation, and strain localization [3]. Conventional models, whether

* Corresponding authors.
E-mail addresses: weizhao0120@nuaa.edu.cn (W. Zhao), mqwei@nuaa.edu.cn (M. Wei).

https://doi.org/10.1016/j.compstruct.2025.119910
Received 28 August 2025; Received in revised form 19 November 2025; Accepted 29 November 2025
Available online 1 December 2025

analytical or empirical, often rely on idealized geometric assumptions or homogenization theories that ignore the intrinsic disorder and asymmetry present in real materials [9]. Mishra et al. illustrated the energy absorption of multiple aluminum foam-filled tubular cores sandwiched between two plates using numerical simulations, indicating the influence of the placement of the core on the energy absorption properties [10]. Zhao et al. employed ABAQUS to calculate the energy absorption of expanded polystyrene foam, discussed how parameters such as foam density and thicknesses of the foam and plates influenced the deformation behavior of the specimens [11]. Consequently, these models fail to account for nonlinear deformation mechanisms, including localized buckling, tension–compression asymmetry, and progressive cell collapse, all of which are critical to understanding how AFS structures behave under dynamic or impact loading. More importantly, current methods lack the ability to interpret or quantify how specific microstructural features such as pore size gradients, anisotropy, or topological invariants contribute to macroscopic performance metrics. This constrains both the accuracy of performance prediction and the capacity for the structure-driven design of foams with tailored functionalities. In essence, the field lacks a predictive and interpretable mapping from morphology to mechanics, a capability that is central to data-driven materials discovery and inverse design.

To address these bottlenecks, recent years have witnessed a surge in data-driven modeling approaches, especially those based on machine learning and deep learning [12–14]. Researchers have attempted to predict mechanical properties of porous structures using two-dimensional (2D) and three-dimensional (3D) methods. Zhuang et al. [15] used a 2D Convolutional Neural Network (CNN) combined with the conditional generative adversarial network (GAN) to generate and evaluate synthetic foam structures, which, the 2D-CNN models have been applied to cross-sectional images or slices of aluminum foams to estimate compressive strength or yield stress. Hangai et al. [16] used CT images of aluminum foam to estimate its yield behavior via deep networks. However, 2D-based methods inherently lack the ability to capture three-dimensional spatial complexity, thereby limiting their expressiveness for predicting 3D mechanical phenomena. As a remedy, Wang et al. [17] adopted 3D-CNN architectures to vocalize porous structures and model the relationship between 3D geometry and material response and demonstrated thermal property prediction. Zhuang et al. [18] achieved the prediction of the stress–strain response for voxelized aluminum foam models using 3D-CNN models, and the Thiessen polygon was utilized to simplify the actual structure. Despite their improved performance over 2D-CNNs, these methods suffer from serious limitations: (1) significant computational and memory burdens due to dense voxelization of void-rich structures, (2) trade-offs between voxel resolution and model accuracy, and (3) inefficiencies in training convergence and generalization. Consequently, existing CNN-based models are constrained in resolution, scalability, and ability to preserve fine mesostructural detail.

Critically, these existing approaches, whether empirical or data-driven, still struggle to bridge the macro–micro structural gap and to provide a theoretical understanding of how geometric features dictate energy absorption characteristics. There remains a lack of models capable of capturing rich mesoscale structural features and translating them into interpretable and predictive macroscopic performance measures.

Recently, point cloud learning has shown remarkable success in diverse 3D modeling tasks, particularly in computer vision, medical imaging, and additive manufacturing [19–21]. In the cause of topology optimization and computational mechanics, point cloud neural networks have shown a strong ability to capture the deformation behaviors of complex lattice structures and printed porous scaffolds [22], which underscore the potential of the method in learning geometric–functional relationships from irregular and sparse 3D data. Despite these advances, point cloud learning has not yet been applied to AFS materials, where the complex structure of the foam core with random pore distribution, partial defects, and non-uniform connectivity presents unique challenges for modeling. Traditional voxel or mesh-based methods often struggle to retain detailed pore-scale features while maintaining computational efficiency, leading to trade-offs between resolution and practicality [18]. In contrast, point cloud representations naturally conform to the sparse, nongrid-like nature of porous structures, enabling efficient encoding of their mesoscopic morphology with minimal redundancy. In addition, point cloud networks such as PointNet [19] and its variants are capable of directly learning from unordered point sets, which makes them particularly suitable for modeling the stochastic architecture of foam core. These networks offer hierarchical feature extraction and long-range spatial dependency modeling, which are critical to capturing how distributed pore geometries collectively influence global energy absorption behavior, a central but unresolved question in current AFS material modeling.

By introducing point cloud learning into this domain, this work pioneers a new paradigm for structure–property prediction in space porous materials. Specifically, we introduce a new 3D representation of the pore-level, termed the pore cloud, in which the aluminum foam core is described as a 3D point cloud derived from CT scans. In conjunction with finite element-based energy absorption labels, a new network architecture (PoreNet) is constructed to learn the mapping of mesostructural geometry to macroscopic performance. This framework not only avoids the inefficiencies of voxel-based CNNs, but also enables bottom-up structure–property learning, paving the way for interpretable, data-driven design of porous sandwich materials. By bridging mesoscopic geometry with macroscale mechanical response through efficient point cloud learning, this research lays the foundation for the next generation of performance prediction, inverse design, and material optimization in advanced structural composites.

2. Method

In this work, a deep learning model is proposed to predict the energy absorption of porous sandwich structures. As shown in Fig. 1, the framework consists of the following three components:

(1) **Dataset construction**. Initially, CT scans of actual aluminum foam samples are conducted to generate cross-sectional images, enabling reconstruction of pore clouds. Next, we reconstruct the 3D foam structure from CT images and bond it with face sheets to sandwich panels. Subsequently, finite element analysis (FEA) is performed under compression to simulate the stress–strain behavior, and the energy absorption curve is obtained by integrating the stress over the strain. The resulting paired pore clouds and curves can be used to train the energy absorption prediction model, which links the core structure to its mechanical response. The data set is divided into 85% for training/15% testing, and data augmentation techniques are applied to improve robustness.

(2) **PoreNet design and training**. PoreNet is a point cloud-based neural architecture designed with local and global enhancement modules, integrated via a cross-attention fusion mechanism. Feature aggregation is achieved through a global max-pooling operation built on Multi-Layer Perceptron (MLP) layers. This architecture effectively fuses mesoscopic and macroscopic information.

(3) **Model validation**. The trained model is assessed on the test samples by comparing the predicted and actual performance to validate its effectiveness. The generalization ability of the proposed framework is further assessed to verify its robustness and applicability to practical use cases.

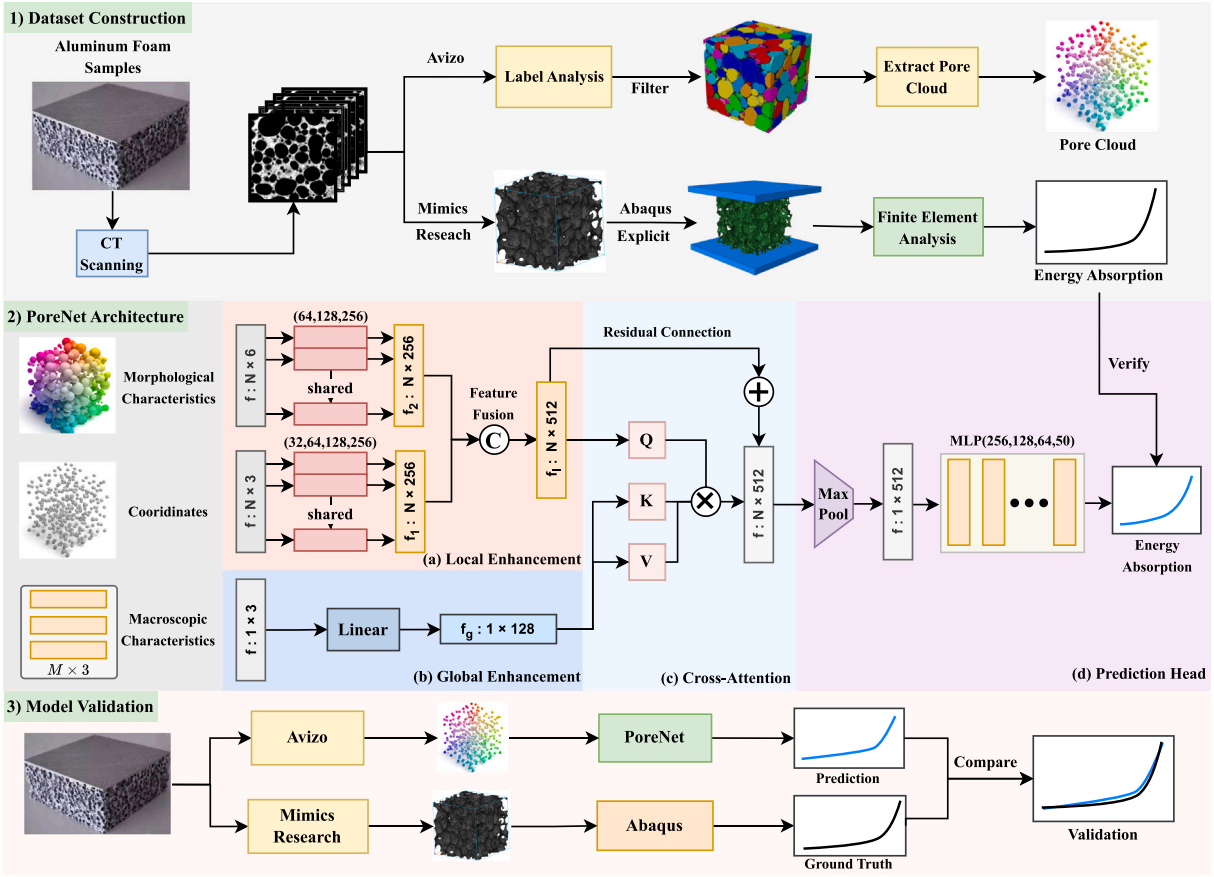

Fig. 1. Overview of the proposed framework for predicting energy absorption in porous sandwich structures using a point cloud based network. (1) Dataset construction: High-fidelity 3D pore clouds are generated from real aluminum foam samples via 3D scanning and paired with finite element analysis (FEA)-based energy absorption data. (2) Prediction network (PoreNet): A deep learning model based on 3D pore clouds, incorporating a multi-layer perception (MLP) architecture. The numbers in parentheses denote the dimensions of each MLP layer.

2.1. Pore cloud representation

Extracting appropriate features from complex 3D pore structures is a key to predicting and optimizing mechanical properties. The pore structure of the sandwich core exhibits significant randomness and non-structural characteristics, with its spatial distribution being the most critical structural feature. Once the pore structure of a foam aluminum core is determined, its overall geometric properties are also defined. The 'Pore Cloud' is introduced as an enriched 3D point cloud representation, inspired by recent developments in 3D vision, to model complex pore structures more effectively. Mathematically, a point cloud can be expressed as $\mathbf{P} = \{\mathbf{p}_i\}_{i=1}^{N}$, where N is the total number of points, and each point $\mathbf{p}_i = (x_i, y_i, z_i)$ is defined by its 3D coordinates. By treating each pore as a point in a point cloud and extracting structural parameters such as pore size, porosity, and cell thickness as point features, the pore structure can be represented as a set of points with associated feature information. Specifically, the pore cloud $\mathbf{P}_f$ can be represented as Eq. (1):

$$\mathbf{P}_f = \{(\mathbf{p}_i, \mathbf{f}_i)\}_{i=1}^{N}, \tag{1}$$

where each pore contributes a point $\mathbf{p}_i$ and associated structural features $\mathbf{f}_i$, including volume, surface area, equivalent diameter, anisotropy, orientation angles, and sphericity.

This representation avoids limitations of 2D representations and inefficiencies of voxel-based methods, providing a fast, accurate, and comprehensive method to predict the performance of foam sandwich structures.

2.2. Dataset construction

The performance of the deep learning model is highly dependent on large-scale, high-quality, and well-distributed data sets with complete feature information. Previous studies on porous metals are often constrained by data scarcity, leading to simplified modeling approaches. Some of them simplify the modeling by reducing the structure to a 2D representation [23], while others randomly generate structures within a defined range of parameters [18]. These factors limit the predictive accuracy and generalization capability of the models.

To more accurately capture the 3D morphology of porous sandwich structures and enhance the prediction of their energy absorption behavior, a large-scale dataset is constructed to support the development of high-performance deep learning models. In this study, AFS structures are chosen as the representative material system due to their widespread use and well-documented mesostructure characteristics. The constructed data set captures both the mesoscopic features of the pore and the corresponding macroscopic mechanical responses, providing a reliable foundation for model training and validation. In total, the data set comprises 844 real samples obtained from CT-scanned AFS structures. After applying data augmentation techniques, 2181 samples are used for training, and an independent set of 117 samples is reserved for testing.

2.2.1. Extraction of pore clouds

The data set was constructed by using real AFS samples. The aluminum foam core was prepared via the melt-foaming method using commercially pure aluminum (≥ 99.9 wt%) as the substrate material.

Porosity	Original Sample	CT Scan	3D Reconstruction
High ~80%	(a) 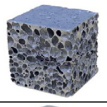	(b) 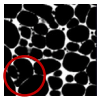	(c) 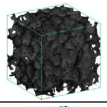
Medium ~70%	(d) 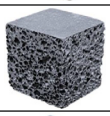	(e) 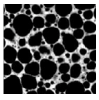	(f) 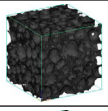
Low ~50%	(g) 	(h) 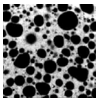	(i) 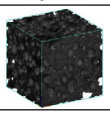

Fig. 2. CT imaging and 3D reconstruction of AFS samples with varying porosity levels. (a)–(c) Samples with ~80% porosity, (d)–(f) ~70% porosity, and (g)–(i) ~50%. Naturally occurring defect structures within the material are also captured in the dataset, as indicated by the red circles in (b).

To prepare the foam, approximately 2 wt% calcium was first added to the molten aluminum to increase viscosity and stabilize the system. Afterward, 1–2 wt% titanium hydride (TiH_2) was incorporated as the blowing agent, decomposing to release hydrogen and produce the cellular structure [24]. After foaming under controlled conditions, the material was cooled to obtain the solid aluminum foam with porosities ranging from 40% to 90%. The face sheets were manufactured from AlSi10Mg alloy (yield strength is 200 MPa) and subsequently bonded to the foam core using a two-component structural polyurethane adhesive commonly employed for metal–foam laminates.

High-resolution CT scans (70 μm) are employed to capture detailed 3D images of samples with porosities ranging from 40% to 90%. This non-destructive technique provides high-resolution volumetric data, effectively capturing key mesoscale and macroscale features such as porosity, pore morphology, and distribution within the aluminum foam. Fig. 2 shows examples of the original aluminum foam samples, the corresponding CT scan images, and 3D reconstructions.

From the CT scans, we extract uniformly sized cubic sub-samples, each composed of 200 slices of 200 × 200 pixels, corresponding to a physical size of 14 × 14 × 14 mm. Subsequently, an analysis is performed using the Label Analysis in Avizo software to extract the pore features. To ensure that the pore morphology is comprehensively and quantitatively characterized, maximizing the structural representativeness of each pore and including geometric, morphological, and orientational attributes, the following six key pore features are identified:

- **Volume**, defined as the total voxel count of the pore:

$$V = VoxelCount \times c_x \times c_y \times c_z \tag{2}$$

- **Surface area**, measured by the area of the pore boundary:

$$Area = \int_{\delta X} \sqrt{x'^2 + y'^2 + z'^2}\, dt \tag{3}$$

- **Equivalent pore diameter**, representing the diameter of a sphere with the same volume as the pore:

$$EqD = \sqrt[3]{\frac{6 \times V}{\pi}} \tag{4}$$

- **Anisotropy**, measuring the deviation of a region from a spherical shape as:

$$Ani = 1 - \lambda_{\min}/\lambda_{\max} \tag{5}$$

where $\lambda_{\min}$ and $\lambda_{\max}$ are the minimum and maximum eigenvalues of the covariance matrix, respectively. The elements of the covariance matrix are derived from the coordinate distribution of the particles.

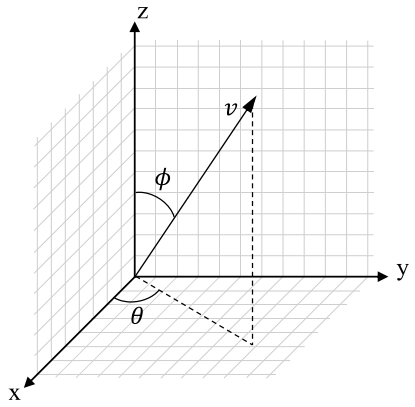

Fig. 3. Definition of orientation angles in 3D space. The azimuth angle θ represents rotation around the vertical axis, while the polar angle ϕ measures the deviation from the z-axis.

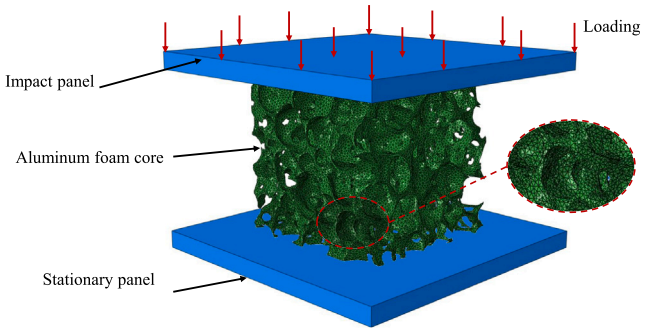

Fig. 4. Finite element model for high-velocity dynamic compression of AFS structures. The model simulates impact behavior to generate ground-truth energy absorption values for training and evaluating the proposed learning framework.

- **Pore orientation**, determined by the principal direction in which the particle distribution is most elongated, corresponding to the largest eigenvector of the covariance matrix. This orientation is expressed as the azimuth angle θ and the polar angle ϕ, as shown in Fig. 3. θ is the azimuth angle, measured between the projection of the main axis onto the xy plane and the positive X axis, ranging from −180 ° and +180 °. ϕ is the polar angle, measured from the positive Z axis, ranging from 0 ° to 90 °.
- **Sphericity**, quantifying how closely a pore approximates a spherical shape:

$$Sph = \frac{\pi^{1/3} \cdot (6 \cdot V)^{2/3}}{Area} \tag{6}$$

The center coordinates and the above six features constitute the pore cloud representation in Eq. (1). In addition, we calculate several macroscopic characteristics that significantly impact mechanical properties, which can be incorporated into the model as monitoring variables, enhancing its predictive capability. Specifically, the fractal dimension and the average cell wall thickness of the samples are calculated using the BoneJ plugin in ImageJ 1.54f, while the porosity is obtained from Avizo.

2.2.2. Energy absorption simulation

3D models of aluminum foam are reconstructed from CT scans using Mimics Research 20.0. Given that aluminum foam models are not sensitive to the size of the element [25], tetrahedral elements (C3D4) with a maximum size of 0.4 mm are used for meshing to improve

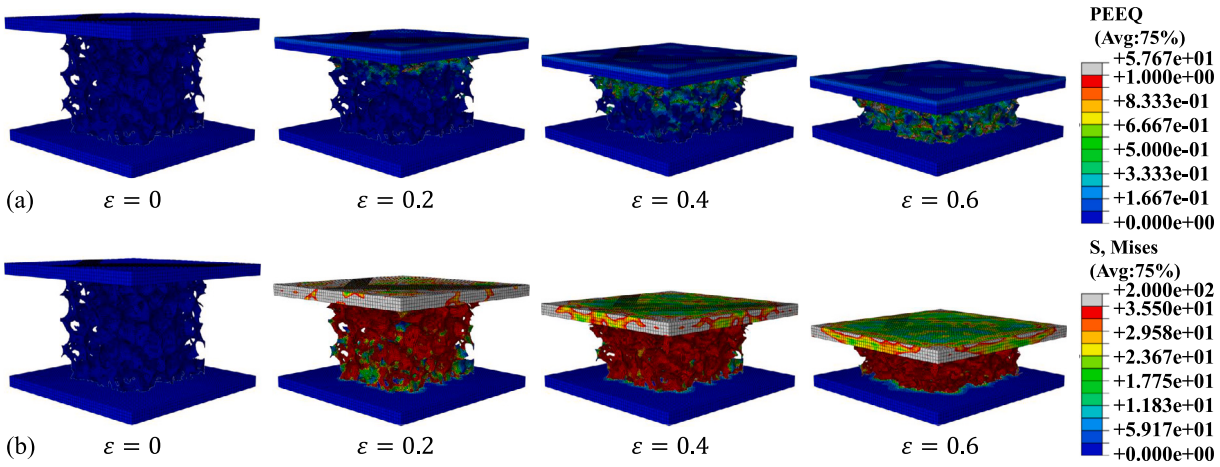

Fig. 5. Finite element simulation results of an AFS structure (porosity: 81%) under dynamic compression. (a) Equivalent plastic strain (PEEQ) contours showing localized deformation patterns within the structure. (b) The von Mises stress distribution illustrating stress concentration and load transfer during the compression process.

Table 1
Material properties of the cell wall in AFS structures. Both the panel and core share the same base material properties (aluminum), with differing yield strengths due to structural differences.

Part	Density ρ_s (kg/m^3)	Elastic modulus E (MPa)	Poisson's Ratio ν	Yield strength σ_y (MPa)
Panel Metal	2700	70,000	0.33	200
Core Metal	2700	70,000	0.33	35.5

computational efficiency. A finite element model of dynamic compression is then established using Abaqus 2022/Explicit. As shown in Fig. 4, aluminum panels are first bonded to the aluminum foam, followed by explicit dynamic analysis to simulate the mechanical performance of the foam sandwich structure under impact loads. Specifically, the assembly model consists of three parts: two aluminum panels located at both ends of the foam in the Z direction and an aluminum foam core. The panels (24 mm × 24 mm × 1.5 mm) are sized to fully cover the foam core. The degrees of freedom of the stationary panel are fully constrained. The upper surface of the panel impacts the sample at a fixed velocity of 100 m/s, where the accuracy of Abaqus simulations under high-speed impact conditions has been validated in previous studies [26]. The foam matrix, produced by foaming technology, is approximated by pure aluminum. An ideal elastoplastic model is employed to characterize the cell wall material of the foam, which is assumed to be composed of pure aluminum. The yield strength of the base material is defined as 35.5 MPa [27,28]. The material of the panels is assumed to be an aluminum alloy and the yield strength is set at 200 MPa. The material parameters for the aluminum panels and the base material matrix are shown in Table 1.

Penalty friction contact (with a coefficient of 0.2) and hard contact are defined between the foam and the panels, as well as between the foam cell walls. A time step of 0.0001s is set, resulting in a total compression of 10 mm, corresponding to an overall compressive strain of approximately 0.71. The compression deformation process of an AFS sample is illustrated in Fig. 5. It can be observed from the equivalent plastic strain (PEEQ) contours that plastic deformation progressively gains from the impact contact region at the top and gradually propagates downward as the strain increases. In particular, when the nominal strain reaches approximately 0.2, plastic yield occurs across the entire foam core, indicating the onset of overall yielding, although localized plastic deformation develops sequentially from the top surface.

The total loads on the AFS samples with various porosities are obtained based on the reaction force on the stationary surface. The nominal stress and strain are then calculated using the total load and the displacement at the impact end, which are used to generate the stress–strain curves.

Energy absorption per unit volume (EAUV) is used to evaluate the energy absorption performance of AFS [23]. EAUV can be calculated by integrating the stress–strain curves as follows:

$$C = \int_0^{\varepsilon} \sigma(\varepsilon) d\varepsilon \approx \sum \frac{\varepsilon_{i+1} - \varepsilon_i}{2} (\sigma_{i+1} + \sigma_i), i = 0 \cdots n \tag{7}$$

where C is the energy absorption per unit volume, σ is the stress, and ε is the strain.

2.2.3. Pre-processing and augmentation

Before data is fed into the neural network for training, preprocessing is required, including dimension unification and data normalization. This ensures a consistent distribution of each training batch and improves the stability of the neural network.

Dimension unification. To address varying pore cloud sizes, zero padding is applied to ensure that each sample contains exactly $N = 1024$ points. Specifically, for samples with fewer than 1024 points, zeros are appended to the original feature data until the required N points are reached.

Data normalization. For the volume and surface area features in the pore cloud data, where the scale differences are significant, a logarithmic transformation is applied for normalization, expressed as Eq. (8):

$$x^i_{\text{norm}} = \log(x^i + 1) \tag{8}$$

where x^i represents the original feature ith, and the base is set to 200 in the experiment. For the remaining features (coordinates, diameter, anisotropy, orientation angles, sphericity, fractal dimension, average cell wall thickness and porosity), Min–Max normalization is used as:

$$x^i_{\text{norm}} = \frac{x^i - x^i_{\min}}{x^i_{\max} - x^i_{\min}} \tag{9}$$

where $x^i_{\min}$ and $x^i_{\max}$ denote the minimum and maximum values of the ith feature x^i, respectively.

Due to the initial delay in the stress response under high-speed impact, the FEA output often includes extremely small nonzero values (ranging from 10^{-29} to 10^{-3}). To avoid skewing the learning process, the values below 10^{-5} are cut and log-normalized, that is,

$$y_{\text{norm}} = \frac{\log(y) - \log(y_{\min})}{\log(y_{\max}) - \log(y_{\min})} \tag{10}$$

where y represents the original energy absorption curve, $y_{\min}$ and $y_{\max}$ are the minimum and maximum values of y, respectively.

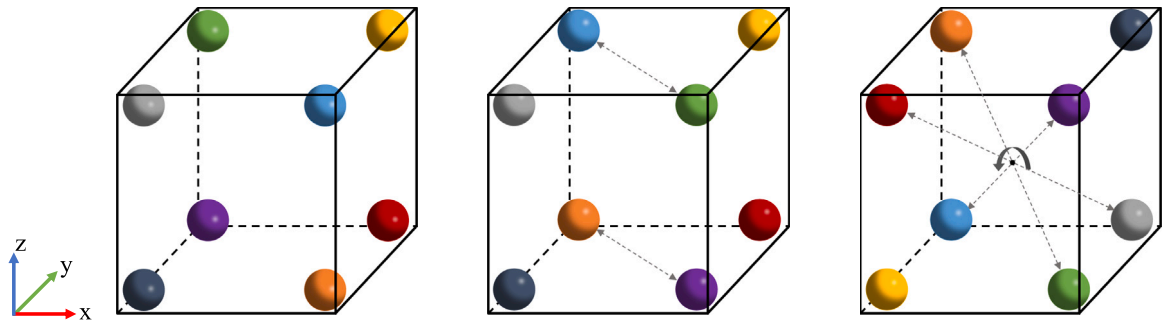

Fig. 6. Illustration of the two data augmentation strategies. The mirror transformation reflects the pore cloud with respect to the plane $y = x$, and the central symmetry transformation reflects each point with respect to the center of the point cloud. For clarity, only the points in the cube corners are shown.

Data augmentation. To further expand the data set and improve the learning capacity of the deep learning model, data augmentation is performed after normalization. Specifically, we apply two geometric transformations, mirroring and central symmetry, to augment the data. The mirror transformation reflects the pore clouds with respect to the plane $y = x$, while the central symmetry transformation reflects each point with respect to the center of the point cloud. Fig. 6 illustrates the two data augmentation strategies applied to the pore cloud representations.

These transformations modify the spatial distribution and orientation of the pores, but preserve their structural and physical characteristics. Since the aluminum foam core is modeled as an isotropic material in this study, it is reasonable to assume that energy absorption remains invariant under these transformations. These enhancement strategies increase data set diversity and promote better generalization in model training. Using this approach, a final training set of 2181 samples is constructed, providing a robust foundation for training deep learning models.

2.3. PoreNet architecture

Fig. 1 outlines the architecture of PoreNet. The model takes as input macroscopic structural descriptors and pore clouds. Macroscopic features are passed through linear layers to extract global features, while the pore clouds are processed by two shared-weight convolutional layers to extract local spatial and morphological features. The extracted local features are then concatenated and fused with global features using a cross-attention mechanism. This fused output is aggregated using max-pooling to produce the final feature representation. In the following, we elaborate on the core components in PoreNet.

2.3.1. Local enhancement module

The local enhancement module is designed to capture fine-grained spatial and morphological features within the pore cloud. The module is also capable of extracting discrete spatial features randomly distributed and defects within the pore structure, which are often difficult to capture using conventional methods. Specifically, the input pore cloud features are split into spatial (coordinates) and morphological (volume, surface area, anisotropy, etc.) components. Two parallel 1D convolutional blocks (with shared weights) are used to learn the initial features, respectively. This structure effectively captures complex and irregular patterns in the pore cloud representation, improving the representation of 3D geometry.

The 1D convolution operation is defined as

$$y_{n,j} = \sum_{c=0}^{C_{\text{in}}-1} \sum_{k=0}^{K-1} w_{j,c,k} \cdot x_{n+k,c} + b_j \tag{11}$$

where $x \in \mathbb{R}^{N \times C_{\text{in}}}$ is the input, $y \in \mathbb{R}^{N \times C_{\text{out}}}$ is the output, n is the spatial index of the input sequence, and j indexes the output channels. $w_{o,c,k}$ is the weight of the kernel, b_o is the bias and K is the kernel size. Each convolutional layer is followed by batch normalization and ReLU activation. In practice, three layers are used for spatial features and four for morphological features, each expanding to 256 dimensions. The resulting 512-dimensional local feature vector is obtained by concatenation.

2.3.2. Global enhancement module

To capture the overall structure of the sample, a global feature extractor is implemented. This module uses four linear layers with ReLU activation to process the macroscopic characteristics, producing a 128-dimensional global representation. These global features help the model learn the relationship between pore structure and mechanical performance.

2.3.3. Cross attention module

To integrate local and global characteristics, a cross-attention mechanism [29] is employed. This mechanism computes weighted global features conditioned on local inputs, helping the model focus on contextually relevant information from different feature types. Specifically, the local features f_l are used as queries (Q), and the global features f_g serve as keys (K) and values (V). The attention computation is defined as:

$$f_{att} = \text{softmax}\left(\frac{QK^T}{\sqrt{d_k}}\right)V \tag{12}$$

where d_k is the dimensionality of the keys. Then, a residual connection is applied by adding the weighted global features to the input local feature to obtain the final overall representation of the feature f:

$$f = f_l + f_{att} \tag{13}$$

This operation helps maintain stable gradients and improves feature integration.

2.3.4. Prediction head

The aggregated features are passed through maximum pooling to produce the 512-dimensional permutation-invariant vector, following the principle used in PointNet [19]. This vector is processed through fully connected layers with L_2 regularization to prevent overfitting.

2.3.5. Loss function

To train the network, a composite loss function is used. Although Mean Squared Error (MSE) loss is commonly used, it is sensitive to outliers and often leads to vanishing gradients. Therefore, L_1 loss is added to improve robustness, and a monotonicity loss is introduced to enforce the physical constraint that energy absorption should increase with strain. The losses are defined as follows:

$$L_{\text{MSE}} = \frac{1}{n}\sum_{i=1}^{n}(y_i - f(x_i))^2 \tag{14a}$$

$$L_{\mathrm{L1}} = \frac{1}{n}\sum_{i=1}^{n}|y_i - f(x_i)| \tag{14b}$$

$$L_{\mathrm{mono}} = -\frac{1}{n-1}\sum_{i=1}^{n-1}\mathrm{ReLU}(f(x_{i+1}) - f(x_i)) \tag{14c}$$

In these loss definitions, y_i and $f(x_i)$ denote the ground truth of energy absorption and the predicted output, respectively. With these loss terms, the final loss function is a weighted sum:

$$L_{\mathrm{total}} = \lambda_1 \cdot L_{\mathrm{MSE}} + \lambda_2 \cdot L_{\mathrm{L1}} + \lambda_3 \cdot L_{\mathrm{mono}} \tag{15}$$

In our experiments, $\lambda_1 = 1$, $\lambda_2 = 0.5$, and $\lambda_3 = 0.2$.

2.3.6. Implementation and training details

PoreNet is implemented in Python 3.10 with PyTorch 2.1.1. The model is trained on an NVIDIA GeForce RTX 3060 GPU (12 GB) and an Intel Core i5-13400 CPU (2.50 GHz). The AdamW optimizer [30] with an adaptive learning rate is employed, using a batch size of 32, an initial learning rate of 0.0031, and a dropout rate of 0.3 in the final layers. The network is trained for 500 epochs. After approximately 25 min of training, the model is able to accurately predict the energy absorption curves of the AFS structures.

3. Results and discussion

3.1. Dataset from mesoscopic structure to macro performance

This study constructed a comprehensive dataset that links the structure characteristics of AFS to their energy absorption behavior. Each entry consisted of mesostructure parameters and macrostructure parameters (pore cloud parameters), the corresponding stress–strain and energy absorption curves of AFS.

The AFS samples (24 mm × 24 mm × 17 mm) cover a wide spectrum of structural configurations. Each sample contains an aluminum foam core (14 mm × 14 mm × 14 mm) with pore counts ranging from 50 to 1000, average cell wall thickness between 0.5 mm and 2.5 mm, and porosity levels from 40% to 90%. On the mesoscale, unit pore counts vary from 100 to 1000, with pore volumes ranging from 0.5 m^3 to 500 m^3 and surface areas from 0.03 m^3 to 630 m^3. This wide variability ensures that the data set captures complex and realistic morphologies, enhancing the robustness of subsequent analysis. The complete data set comprises 844 samples, with 85% allocated for training and 15% for testing. After data augmentation, the training set expands to 2181 samples, while the test set includes 117 samples. The enhancement improves the diversity of features and supports more robust model generalization.

3.1.1. Stress–strain responses and energy absorption results

As shown in Fig. 7, eight AFS samples with different porosities were selected to demonstrate their stress–strain responses, which consistently exhibit three stages: elastic, plateau, and densification. After the initial elastic response, transient oscillations occur as a result of stress wave reflections at the boundary of the materials. As compression progresses, the stress reaches a plateau, indicating the onset of plastic deformation, and subsequently rises sharply during the densification stage. A general trend is observed where the lower porosity leads to increased stress levels in all stages of deformation. Notably, samples with similar macroscopic features (e.g., porosity and wall thickness) can exhibit distinct mechanical behaviors. For example, samples (4) and (5) have nearly identical porosities (0.668 and 0.663) and pore counts (573 and 577), yet show significantly different responses. This discrepancy reflects the influence of microstructural randomness. The influence is difficult to capture using conventional metrics. These results underscore the need for data-driven methods to model complex structure–property relationships.

All strain onsets in Fig. 7 occur at 0.012. The reason is that there is a brief delay in the stress–strain response due to the time it takes for the elastic wave to reach the fixed surface. Stress development begins at a strain of approximately 0.012, as calculated by [31]:

$$\varepsilon_{ini} = v_i / v_e, \tag{16}$$

where v_i is the loading velocity and v_e is the elastic wave speed in the material.

This study focuses on the resilience and plateau phases; therefore, strains up to 0.6 are considered. The energy absorption curve of each sample was discretized into 50 uniformly spaced strain intervals, resulting in a 50-dimensional vector that serves as the prediction target for the model (see Fig. 8). This formulation enables a high-dimensional regression task, allowing the model to learn the full energy absorption profile rather than a single scalar output.

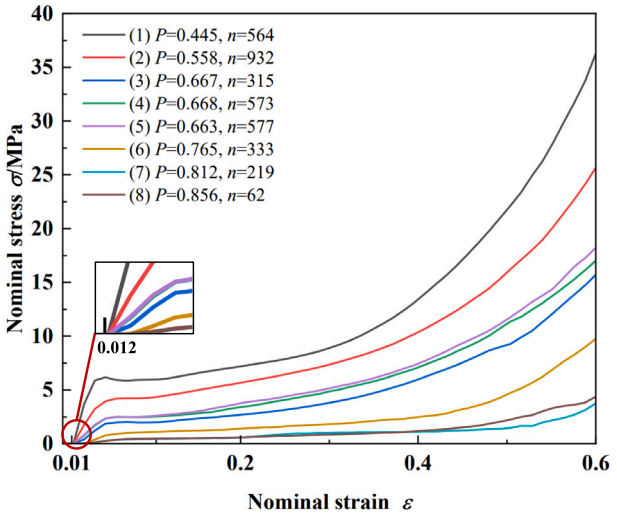

Fig. 7. Stress–strain curves of AFS samples various with porosities and pores number. ρ: porosity, n: number of pores.

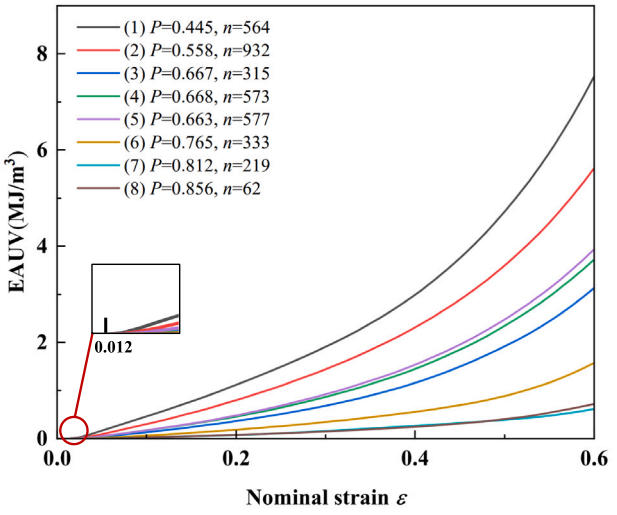

Fig. 8. Energy absorption curves of AFS samples with varying porosities and macroscopic parameters.

3.2. Training and prediction

As shown in Fig. 9, the loss values in both the training and test sets decrease steadily and converge by epoch 500. The total loss decreases steadily, with both training and test losses converging, indicating a good generalization performance of the PoreNet model. The final loss

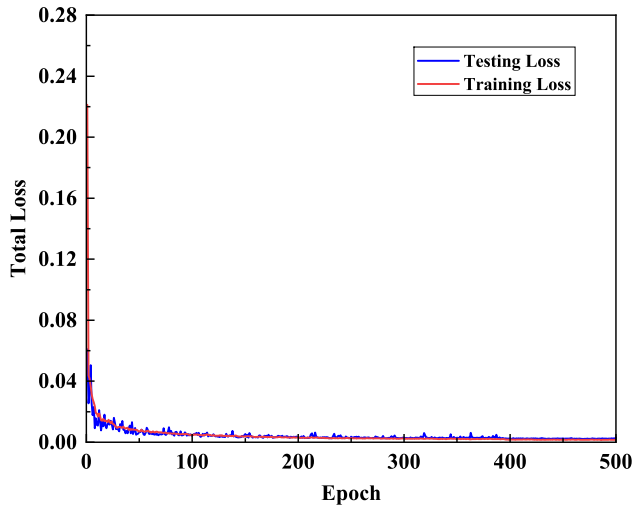

Fig. 9. Training and test loss curves over training epochs.

values are 0.0016 for training and 0.0021 for testing, indicating a strong fit of the model and minimal overfitting [32].

To quantitatively assess model performance, this work employs the Mean Absolute Error (MAE) and Mean Absolute Percentage Error (MAPE) as evaluation metrics, defined as [33]:

$$\boldsymbol{MAE} = \frac{1}{n}\sum_{i=1}^{n}\left|y_i - f\left(x_i\right)\right| \tag{17}$$

$$\boldsymbol{MAPE} = \frac{1}{n}\sum_{i=1}^{n}\left|\frac{y_i - f\left(x_i\right)}{y_i}\right| \times 100\% \tag{18}$$

where y_i and $f\left(x_i\right)$ denote the ground truth and predicted energy absorption values at the strain level i, respectively, and n is the total number of prediction points.

The model based on the test set achieves an average MAE of 0.017 and a MAPE of 2.94%, demonstrating high predictive precision across the full strain range. Both error metrics remain consistently low across all 50 predicted strain intervals, indicating the model's ability to capture subtle variations in the energy absorption response.

Table 2 summarizes the performance of PoreNet, with a test MAE of 0.0174 MPa and a MAPE of 4.88%. As shown in Figs. 10a and 10b, the distribution of MAE and MAPE across the 117 test samples approximates a normal distribution, indicating stable and consistent prediction performance.

However, a single high-energy absorption sample was identified as an outlier, with an MAE of 0.0883 MPa and a corresponding MAPE of 3.24%. This suggests that while the model performs well overall, predictive accuracy may slightly decrease for samples with extreme structural or mechanical characteristics. Further inspection of the outlier sample reveals that it exhibits unusually higher energy absorption than the real test, probably as a result of a dense and highly interconnected pore structure not well represented in the training distribution. Such edge cases highlight the model's sensitivity to underrepresented structural regimes and emphasize the importance of data set diversity.

To address this, future work may incorporate targeted data augmentation or sampling strategies to better cover high-energy structural configurations. Additionally, incorporating structure-aware weighting schemes or uncertainty estimation could improve the model's robustness and interpretability when encountering structurally atypical inputs.

Figs. 11 and 12 provide a comprehensive comparison between predicted and simulated energy absorption curves in a variety of mesostructural configurations. These results collectively demonstrate the high accuracy and generalization capability of the proposed PoreNet framework, particularly in capturing subtle variations arising from mesostructural differences.

Table 2
Prediction errors for energy absorption on the test dataset using the proposed PoreNet model.

Metric	Mean	Min	Max
MAE (MPa)	0.0174	0.0020	0.0883
MAPE (%)	4.88	0.94	25.82

Fig. 11 presents five representative cases (a–e) in which samples exhibit similar porosities but differ in pore counts. This setup is designed to assess the model's sensitivity to internal geometric complexity under fixed global density. For instance, subfigure (a) compares samples with a porosity around 0.44 but varying pore counts from 594 to 675. The predicted curves closely follow the simulation results, indicating that the model effectively captures the performance variations introduced only by differences in the mesoscopic structure. The subfigures (b)–(e) follow a similar pattern at other porosity levels (0.52, 0.64, 0.66, and 0.77, respectively). A particularly interesting observation occurs in Subfigure (d), where a significant divergence appears in the red curve (sample with 199 pores) compared to those with higher pore counts. This discrepancy reflects the substantial influence of reduced pore number — even at constant porosity — on energy absorption performance. Such variations are well captured by the model, validating its ability to differentiate samples that are macrosimilar but microstructurally distinct.

Fig. 12 shifts the focus to another dimension of mesostructural variation: samples with similar pore counts but different porosities. Again, five representative cases are shown (a–e), with each subplot illustrating a fixed pore count range (e.g., around 180–250) and increasing porosity levels. In subfigure (a), all samples have approximately 180 pores, while porosity varies from 0.30 to 0.40. The predicted curves reflect the natural trend that higher porosity generally leads to lower energy absorption. In particular, it captures both macro-level trends and finer structural differences such as relative ordering and nonlinear deformation characteristics. The subfigures (b)–(e) extend this observation to higher pore count groups, with similar consistency between predicted and simulated responses.

Together, these two figures highlight the ability of PoreNet to learn the coupled influence of mesostructural and macroscopic descriptors, including pore size, orientation, count, and porosity, on macroscopic mechanical behavior. Unlike conventional approaches that rely primarily on global parameters (e.g., relative density) [34,35], PoreNet utilizes rich geometric information embedded in the 3D pore cloud to enable high-fidelity predictions across a wide spectrum of structural configurations. This confirms the effectiveness of the model in bridging meso-to-macro scale interactions and its potential as a predictive tool for porous material design.

3.3. Feature map interpretation

To interpret the models' learned representations, this work visualized the pore-level features extracted from the max-pooling layer of the PoreNet architecture (Fig. 13). In this visualization, each pore is represented as a sphere, where the sphere size corresponds to the actual pore volume, and the color intensity encodes the magnitude of the extracted feature, serving as a proxy for the importance of the feature.

In general, larger pores tend to exhibit higher feature values, which aligns with physical expectations given their dominant role in deformation and energy absorption. Furthermore, the model also assigns significant importance to smaller pores in specific configurations, suggesting that it captures more intricate structural dependencies beyond simple size-based heuristics. This reflects the capacity of the network to model nonlinear interactions between spatially distributed pores, including local clustering effects, connectivity, and arrangement.

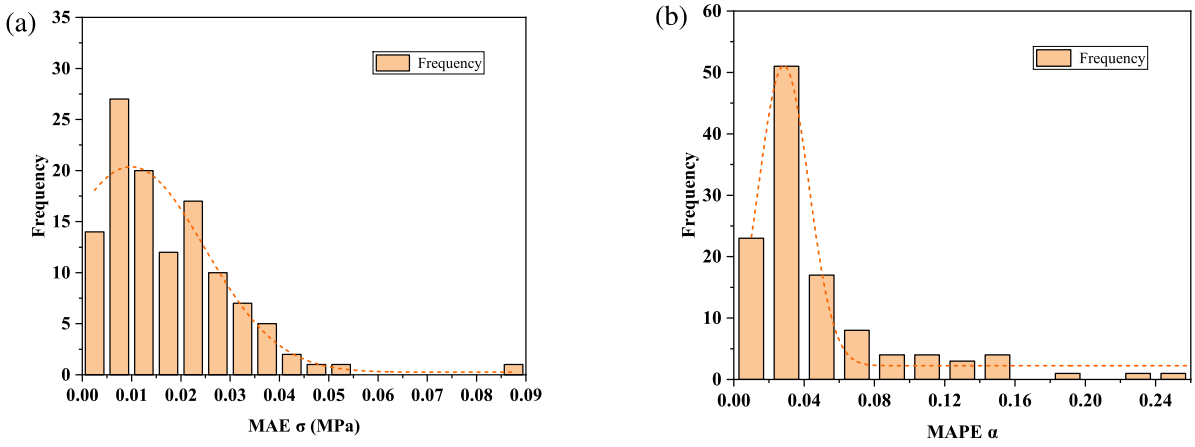

Fig. 10. The histograms of error distributions. (a) Histogram of MAE distribution. (b) Histogram of MAPE distribution.

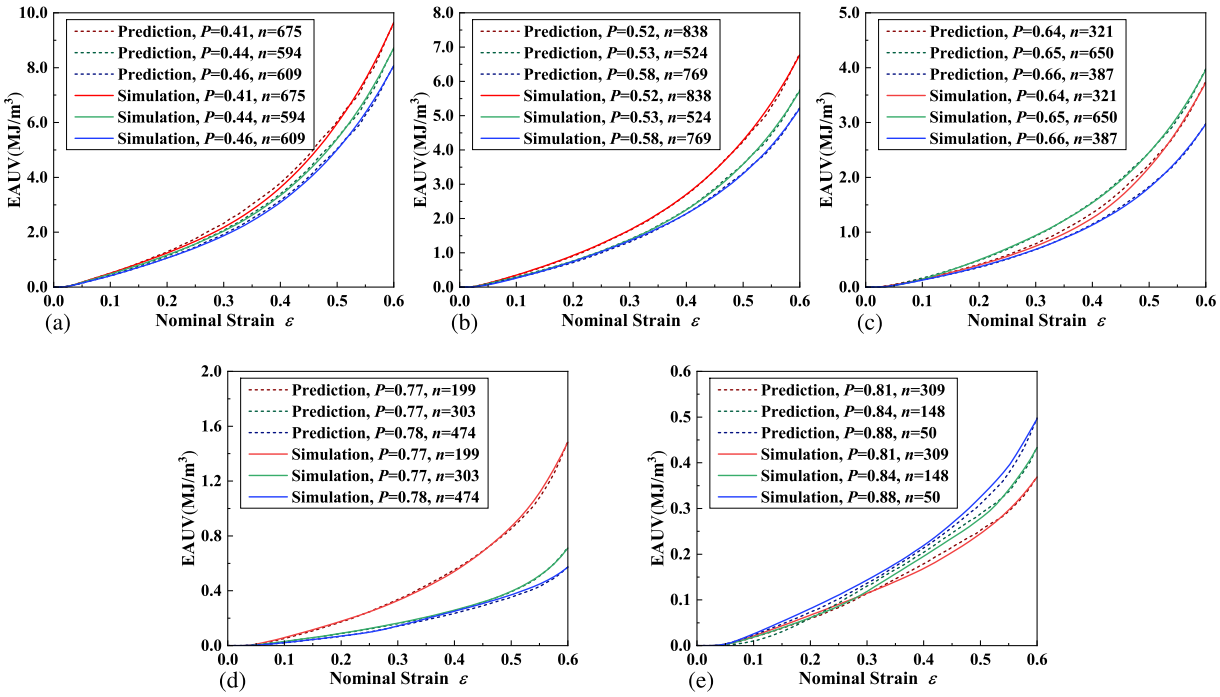

Fig. 11. Comparison of actual and predicted energy absorption curves across varying porosities and pore counts. The figure highlights discrepancies between predicted and actual values for samples with similar porosities but different pore counts.

The consistent identification of intuitive and non-obvious structural contributors highlights the strength of deep learning approaches in learning complex, high-dimensional representations that traditional descriptors may overlook [36].

3.4. Robustness test

Two types of input corruptions during training were introduced to evaluate the robustness of PoreNet: (1) Perturbation, Gaussian noise was added to the pore cloud features and corresponding energy absorption values; (2) Insertion, uniformly distributed outlier points were injected into the input space to simulate structural contamination.

As illustrated in Fig. 14(a), under a moderate noise level of $\sigma = 0.04$, most prediction deviations remain within 8%, and the model maintains a predictive accuracy greater than 90%. Even when 20% of the input points are replaced by outliers, the model still achieves an accuracy exceeding 80%.

Accuracy is defined as the proportion of predicted energy values that falls within a 10% relative error margin across all strain intervals evaluated. These results confirm the strong robustness of PoreNet against both feature-level perturbations and structural outliers, underscoring its applicability in real-world scenarios where measurement noise or partial defects are inevitable.

3.5. Discussion

Deep learning methods exhibit significant advantages in predicting the energy absorption behavior of AFS structures. Traditional homogenization-based constitutive models [43–46] average the inherent stochasticity of the pore structures using empirical parametric formulations, limiting their predictive accuracy for AFS with complex porous core. Although conventional machine learning approaches partially mitigate this limitation by manually selecting features, they rely on predefined descriptors that may overlook critical structural details. As given in 3, methods are compared based on the input data format

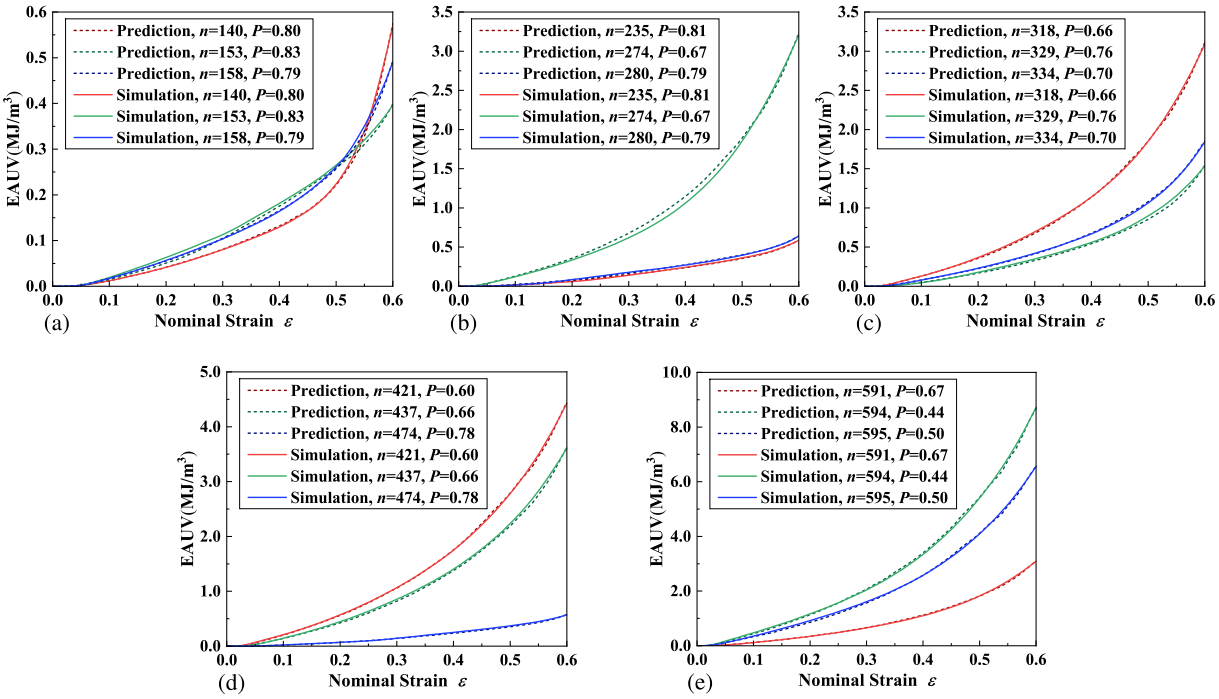

Fig. 12. Comparison of actual and predicted energy absorption curves for samples with similar pore counts but varying porosities.

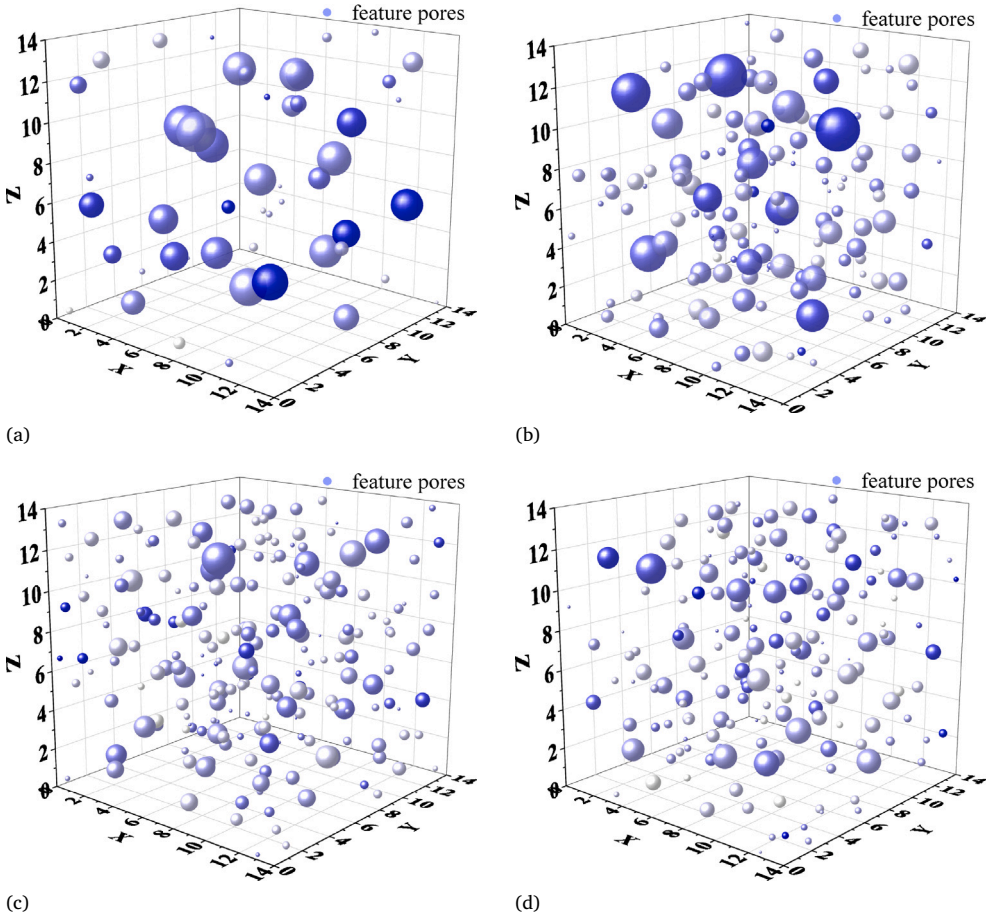

Fig. 13. Feature maps showing spatial locations, sizes, and learned importance of pores. A darker color indicates a larger feature value. In (a) and (b), darker colors tend to correspond to larger pores, whereas (c) and (d) show many small, dark pores, highlighting the importance of their topological structure.

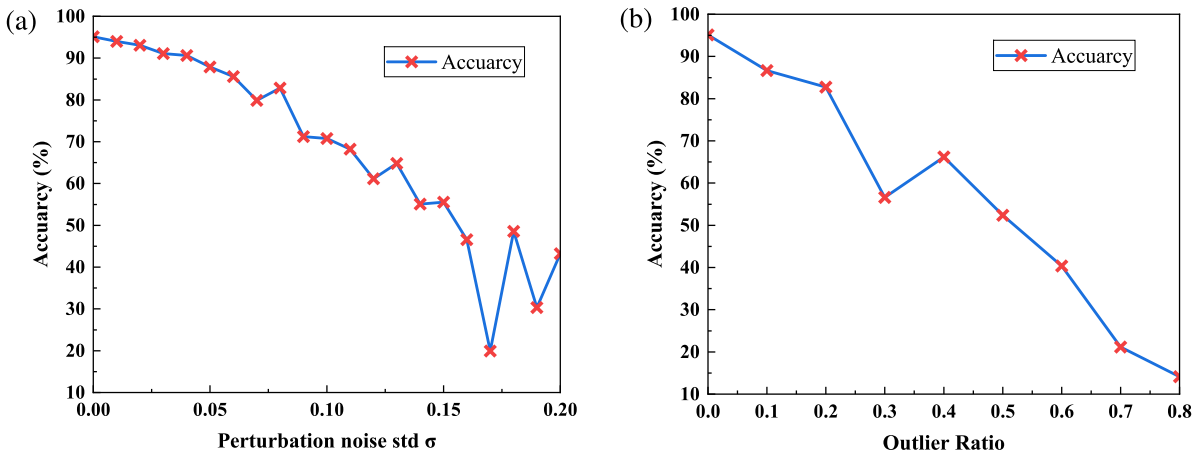

Fig. 14. PoreNet robustness under input corruptions. (a): Gaussian noise. (b): Outliers insertion.

Table 3
Comparative analysis of constitutive modeling (CM) and machine learning approaches for predicting the mechanical behavior of foam materials.

Method	Data format	Approach	Meso-struct.	Model input	Predicted output	Data source	Metrics
[37]	2D	2D-CNN	✓	$I(x,y) \in \mathbb{R}^{H\times W}$	σ_{plat}	Real	Uncertain
[38]	3D	MLP	–	$\frac{\rho^*}{\rho_s}$, d_{avg}, α_{ani}	$\sigma_{\text{plat}}/E/W_{\text{abs}}$	Real	$R^2 = 0.93$
[39]	2D	2D-CNN	✓	$I(x,y) \in \mathbb{R}^{H\times W}$	E/σ_{plat}	Synthetic	$R^2{}_E = 0.88$ $R^2{}_\sigma = 0.59$
[18]	3D	3D-CNN	✓	$\mathcal{V}_{voxel} \in \mathbb{R}^{D\times H\times W}$	$\sigma(\varepsilon)/\varepsilon_{\text{dens}}$	Synthetic	MAPE: 2.90% MAE: 0.3596
[40]	2D (Simplified)	CM+NN	–	ε_{ij}, $i,j \in \{1,2\}$	$\sigma_{ij}(\varepsilon_{ij})$	Synthetic	Lower than 2%
[41]	3D	CM	–	$\frac{\rho^*}{\rho_s}$, $\dot{\varepsilon}$, σ_{ys}	$\sigma^{\text{dyn}}_{\text{plat}}$	Real	Uncertain
[34]	3D	CM	–	$\frac{\rho^*}{\rho_s}$, $\phi_{\text{solid\_frac}}$, σ_{ys}	E/σ_{plat}	Synthetic	Uncertain
[35]	3D	CM	–	$\frac{\rho^*}{\rho_s}$, $\frac{\dot{\varepsilon}_{avg}}{\dot{\varepsilon}_{ref}}$, ε	$\sigma(\varepsilon)$	Real	Uncertain
[42]	3D	CM	–	ρ, T, ε	$\sigma(\varepsilon)$	Real	Uncertain
Ours	3D	**PoreNet**	✓	$\mathcal{P}_{\text{pore}}$, $\mathcal{F}_{\text{macro}}$	$W_{\text{abs}}(\varepsilon)$	Real	MAPE: 4.88% MAE: 0.0174

(2D/3D), the modeling approach (e.g. CM, MLP, CNN), mesostructural features, prediction targets, data sources (real or synthetic), and reported performance metrics. The proposed PoreNet method outperforms existing approaches in terms of multiple aspects in experimental data.

The proposed PoreNet framework addresses these challenges through a novel *pore cloud* representation. This approach explicitly preserves the full randomness of the mesostructure by encoding each pore as a node with spatial coordinates, geometric properties, and topological features. Unlike prior deep learning models that rely on 2D projections (which artificially enforce uniformity) or memory-intensive 3D voxel grids (which lose detail at low resolution), PoreNet builds direct structure–property relationships at the pore level.

This is achieved using parallel local–global feature enhancement modules and cross-attention fusion, enabling the model to learn how groups of pores influence energy absorption. This network is sensitive to small changes in local structure and because of the sparsity of point clouds, it maintains high computational efficiency. The end-to-end learning paradigm autonomously identifies complex, high-dimensional relationships between pore architecture and mechanical response, outperforming traditional and existing deep learning methods, especially when dealing with variable porosity and structural complexity. A detailed comparison with other existing methods is presented in Table 3.

An additional strength of PoreNet lies in its scalability and generalizability. Although this work focuses on AFS structures, the approach is readily transferable to other porous metals and closed-cell foam materials. Beyond mechanical metrics such as energy absorption and stress–strain response, the pore cloud representation can be adapted to predict properties, including damping behavior, thermal conductivity, and temperature fields, positioning PoreNet as a versatile tool for multiproperty prediction in complex porous systems.

In addition to its overall strong performance, there remains room for improvement in the prediction accuracy of PoreNet, particularly in the handling of high-porosity samples. As illustrated in Figs. 15(a) and 15(b), the mean absolute error (MAE) tends to decrease with increasing porosity. This trend arises because high-porosity specimens generally exhibit lower energy absorption, leading to smaller absolute deviations.

However, the mean absolute percentage error (MAPE) remains relatively high for these samples. This is primarily due to the low energy absorption values: even minor prediction errors can result in large relative deviations, thereby inflating MAPE. Additionally, high-porosity structures typically contain fewer pores, resulting in sparser pore cloud representations. When such sparse inputs are aligned into fixed-dimensional arrays during preprocessing, the padding process may introduce redundant or non-informative features that interfere with learning.

To mitigate this, future work may explore improved preprocessing strategies, such as non-zero padding, attention-based masking, or variable-size input handling via transformer architectures. These alternatives have the potential to preserve structural sparsity without introducing artificial bias, and thus represent promising directions for enhancing model robustness across a broader range of porosity conditions.

Despite its strong performance, PoreNet — like most deep learning models — functions as a black box. Although it achieves high predictive accuracy, its interpretability remains limited, making it difficult to quantify the contribution of individual structural features to the

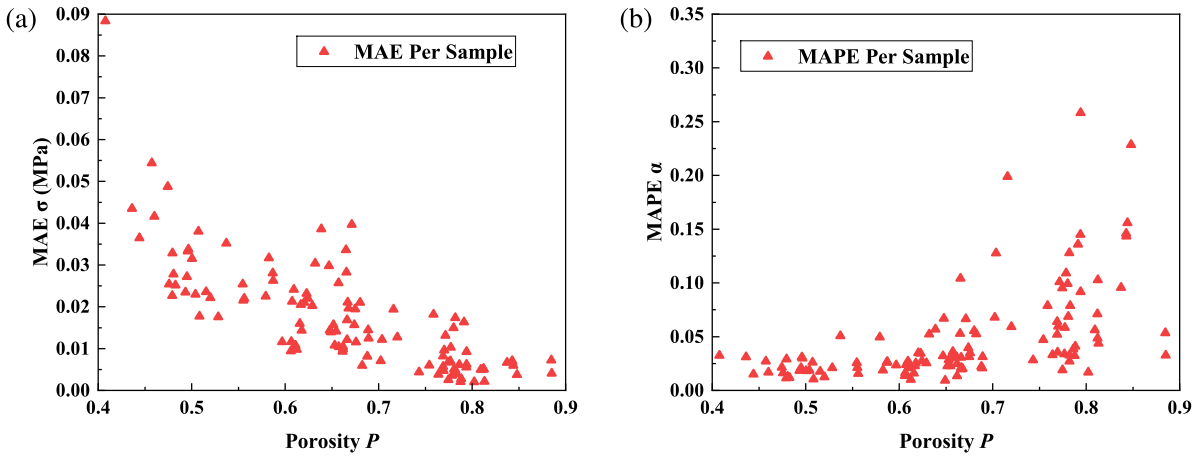

Fig. 15. Distribution of (a) mean absolute error (MAE) and (b) mean absolute percentage error (MAPE) across test specimens with varying porosities.

final prediction. Addressing this limitation through interpretable AI techniques or physics-informed neural networks represents a promising direction for future work.

In summary, the proposed framework provides a flexible and effective solution for predicting multiple properties across a broad spectrum of closed-cell porous materials. Using pore-level geometric and topological information, it allows for accurate, structure-aware modeling of complex cellular architectures. This work underscores the potential of deep learning to transform materials science by facilitating data-driven, interpretable, and scalable approaches to understanding and designing advanced porous systems.

4. Conclusion

This study presents an efficient and generalizable deep learning framework for predicting the energy absorption performance of porous sandwich structures based on a novel pore cloud representation. The proposed method directly incorporates mesoscale geometric and topological information of the porous core, enabling accurate modeling of complex structure–property relationships.

The main conclusions are as follows:

(1) Data Acquisition and Labeling: A high-fidelity data set was constructed using CT-scanned aluminum foam sandwich (AFS) samples. Geometric data at the pores were extracted to form pore clouds, and corresponding energy absorption values were obtained through finite element analysis (FEA). Data augmentation was applied to improve model generalization.

(2) Model Development and Performance: A new neural network architecture, PoreNet, was developed to map the features of the pore cloud to mechanical responses. The model integrates local–global feature encoding and a cross-attention fusion mechanism, enabling it to capture the contribution of individual pores and pore groups. The model achieved a mean absolute error (MAE) of 0.0174 MPa and a mean absolute percentage error (MAPE) of 4.88% on the test set.

(3) Robustness and Efficiency: PoreNet exhibits strong robustness against noise and outlier perturbations, maintaining high prediction accuracy under various corrupted input scenarios. The point cloud-based design also ensures computational efficiency and scalability.

(4) Generalization and application potential: Although validated on AFS, the framework is applicable to a broad class of closed-cell porous sandwich materials. Beyond energy absorption, the approach can be extended to predict other physical properties such as stress–strain response, damping, and thermal conductivity, making it a versatile tool for data-driven design and optimization in advanced composite and cellular materials.

To achieve an efficient and accurate prediction of the energy absorption performance of porous sandwich structures, this study introduces a pore cloud-based representation that effectively captures the mesoscale characteristics of porous cores. Building on this representation, we develop a deep learning framework for energy absorption prediction. Although AFS structures are used as a representative example, the proposed approach is broadly applicable to other porous sandwich structures made of various materials. This work demonstrates the effectiveness of combining pore-level structural representations with deep learning for high-fidelity mechanical property prediction and provides a foundation for future research in AI-guided material design and performance optimization.

CRediT authorship contribution statement

Jiaxiu Zhang: Writing – review & editing, Writing – original draft, Visualization, Validation, Supervision, Software, Resources, Project administration, Methodology, Investigation, Funding acquisition, Formal analysis, Data curation, Conceptualization. **Wei Zhao:** Writing – review & editing, Writing – original draft, Supervision, Project administration, Funding acquisition, Conceptualization. **Ran Chen:** Writing – review & editing, Writing – original draft, Supervision, Software, Investigation. **Liangliang Nan:** Writing – review & editing, Validation. **Wenhao Chen:** Writing – review & editing, Supervision, Project administration, Investigation, Conceptualization. **Mingqiang Wei:** Writing – review & editing, Writing – original draft, Validation.

Declaration of competing interest

We declare that we have no financial and personal relationships with other people or organizations that can inappropriately influence our work, there is no professional or other personal interest of any nature or kind in any product, service and/or company that could be construed as influencing the position presented in, or the review of, the manuscript entitled.

Acknowledgments

This work was supported by the National Natural Science Foundation of China [grant nos. T2322012, 62172218, 62032011] and supported by the Fundamental Research Funds for the Central Universities, China, no. NJ2024029.

Data availability

The data set and the proposed algorithm are publicly available on the project homepage: https://crescentrosexx.github.io/pore-net/.

References

[1] Kulkarni MV, Boppana SB. Composites overview. In: Structural composite materials: fabrication, properties, applications and challenges. Singapore: Springer Nature Singapore; 2024, p. 3–21. http://dx.doi.org/10.1007/978-981-99-5982-2_1.

[2] Song S, Xiong C, Yin J. Mechanical performance of reinforced hybrid periodic-multicell thin-walled structures in sandwich applications: A review. Thin-Walled Struct 2025;208:112832. http://dx.doi.org/10.1016/j.tws.2024.112832, URL https://www.sciencedirect.com/science/article/pii/S0263823124012710.

[3] Ji C, Huang H, Wang T, Huang Q. Recent advances and future trends in processing methods and characterization technologies of aluminum foam composite structures: A review. J Manuf Process 2023;93:116–52. http://dx.doi.org/10.1016/j.jmapro.2023.03.015, URL https://www.sciencedirect.com/science/article/pii/S1526612523002232.

[4] Guo H, Yuan H, Zhang J, Ruan D. Review of sandwich structures under impact loadings: Experimental, numerical and theoretical analysis. Thin-Walled Struct 2024;196:111541. http://dx.doi.org/10.1016/j.tws.2023.111541, URL https://www.sciencedirect.com/science/article/pii/S0263823123010182.

[5] Fan M, Zeng T, Wu R, Cui Y, Xu G, Wang X, Cheng S, Zhao J. Bending behaviors of 3D printed sandwich structures with functionally graded porous lattice cores. Thin-Walled Struct 2025;206:112655. http://dx.doi.org/10.1016/j.tws.2024.112655, URL https://www.sciencedirect.com/science/article/pii/S0263823124010954.

[6] Mallesh S, Hwang J, Choi H, Hong D-J, Seok C, Kwak B, Lee S-Y, Nam Y. Advanced acoustic design: 3D printed thermoplastic folded core sandwich structures with porous materials and microperforations for enhanced sound absorption. Compos Struct 2024;345:118371. http://dx.doi.org/10.1016/j.compstruct.2024.118371, URL https://www.sciencedirect.com/science/article/pii/S0263822324004999.

[7] Yi Z, Si-yuan H, Jia-gui L, Wei Z, Xiao-lu G, Jin Y. Density gradient tailoring of aluminum foam-filled tube. Compos Struct 2019;220:451–9. http://dx.doi.org/10.1016/j.compstruct.2019.04.026, URL https://www.sciencedirect.com/science/article/pii/S0263822318340054.

[8] Wang Z, Hong B, Xian G, Xin M, Huang S, Shen H. Quasi-static and low-velocity impact behaviors of steel-aluminum foam sandwich beams. Structures 2024;64:106549. http://dx.doi.org/10.1016/j.istruc.2024.106549, URL https://www.sciencedirect.com/science/article/pii/S235201242400701X.

[9] Cao S, Ma N, Zhang Y, Bo R, Lu Y. Fabrication, mechanical properties, and multifunctionalities of particle reinforced foams: A review. Thin-Walled Struct 2023;186:110678. http://dx.doi.org/10.1016/j.tws.2023.110678, URL https://www.sciencedirect.com/science/article/pii/S0263823123001568.

[10] Mishra A, Wang Y, Lu J. Energy absorption behavior of a cladding sandwich panel with axially oriented aluminum foam filled tubular cores under impact. Structures 2024;62:106255. http://dx.doi.org/10.1016/j.istruc.2024.106255, URL https://www.sciencedirect.com/science/article/pii/S2352012424004077.

[11] Caliskan U, Apalak MK. Low velocity bending impact behavior of foam core sandwich beams: Experimental. Compos Part B: Eng 2017;112:158–75. http://dx.doi.org/10.1016/j.compositesb.2016.12.038, URL https://www.sciencedirect.com/science/article/pii/S1359836816331523.

[12] Liu J, Huang M, Li Z, Zhao L, Zhu Y. A deep learning method for predicting microvoid growth in heterogeneous polycrystals. Eng Fract Mech 2022;264:108332. http://dx.doi.org/10.1016/j.engfracmech.2022.108332, URL https://www.sciencedirect.com/science/article/pii/S0013794422000911.

[13] Zhang Z, Hong Y, Hou B, Zhang Z, Negahban M, Zhang J. Accelerated discoveries of mechanical properties of graphene using machine learning and high-throughput computation. Carbon 2019;148:115–23. http://dx.doi.org/10.1016/j.carbon.2019.03.046, URL https://www.sciencedirect.com/science/article/pii/S0008622319302702.

[14] Wang M, Wang H, Yin Y, Rahardja S, Qu Z. Temperature field prediction for various porous media considering variable boundary conditions using deep learning method. Int Commun Heat Mass Transfer 2022;132:105916. http://dx.doi.org/10.1016/j.icheatmasstransfer.2022.105916, URL https://www.sciencedirect.com/science/article/pii/S0735193322000380.

[15] Zhuang W, Wang E, Zhang H. Prediction of the compressive mechanical properties and reverse structural design of two-dimensional mesoscopic aluminum foam based on deep learning methods. J Mater Sci 2024;1–24. http://dx.doi.org/10.1007/s10853-024-09866-0.

[16] Hangai Y, Ozawa S, Okada K, Tanaka Y, Amagai K, Suzuki R. Machine learning estimation of plateau stress of aluminum foam using X-ray computed tomography images. Materials 2023;16(5). http://dx.doi.org/10.3390/ma16051894, URL https://www.mdpi.com/1996-1944/16/5/1894.

[17] Wang M, Wang H, Yin Y, Rahardja S, Qu Z. Temperature field prediction for various porous media considering variable boundary conditions using deep learning method. Int Commun Heat Mass Transfer 2022;132:105916. http://dx.doi.org/10.1016/j.icheatmasstransfer.2022.105916, URL https://www.sciencedirect.com/science/article/pii/S0735193322000380.

[18] Zhuang W, Wang E, Zhang H. Prediction of compressive mechanical properties of three-dimensional mesoscopic aluminium foam based on deep learning method. Mech Mater 2023;182:104684. http://dx.doi.org/10.1016/j.mechmat.2023.104684, URL https://www.sciencedirect.com/science/article/pii/S0167663623001308.

[19] Qi CR, Su H, Mo K, Guibas LJ. PointNet: Deep learning on point sets for 3D classification and segmentation. In: Proceedings of the IEEE conference on computer vision and pattern recognition. 2017, p. 77–85.

[20] Qi CR, Yi L, Su H, Guibas LJ. PointNet++: Deep hierarchical feature learning on point sets in a metric space. In: Guyon I, Luxburg UV, Bengio S, Wallach H, Fergus R, Vishwanathan S, Garnett R, editors. In: Advances in neural information processing systems, vol. 30, Curran Associates, Inc.; 2017, URL https://proceedings.neurips.cc/paper_files/paper/2017/file/d8bf84be3800d12f74d8b05e9b89836f-Paper.pdf.

[21] Guo M-H, Cai J-X, Liu Z-N, Mu T-J, Martin RR, Hu S-M. Pct: Point cloud transformer. Comput Vis Media 2021;7:187–99.

[22] Brüel-Gabrielsson R, Ganapathi-Subramanian V, Skraba P, Guibas LJ. Topology-aware surface reconstruction for point clouds. In: Computer graphics forum, vol. 39, (5):Wiley Online Library; 2020, p. 197–207.

[23] Tang M, Wang L, Xin Z, Luo Z. High energy absorption design of porous metals using deep learning. Int J Mech Sci 2024;282:109593. http://dx.doi.org/10.1016/j.ijmecsci.2024.109593, URL https://www.sciencedirect.com/science/article/pii/S0020740324006349.

[24] Zhao W, He S, Wei X, Du Y, Tang G, Zhang Y, Dai G, Gao K, Volkova O. Quantitative relationships between cellular structure parameters and the elastic modulus of aluminum foam. Mater Sci Eng: A 2023;868:144713.

[25] Zhuang W, Wang E. Simulation study on the effect of trapped gas on the dynamic compressive stress enhancement of aluminium foam. Mech Mater 2022;169:104319. http://dx.doi.org/10.1016/j.mechmat.2022.104319, URL https://www.sciencedirect.com/science/article/pii/S0167663622000990.

[26] Guo H, Yuan H, Zhang J, Ruan D. Review of sandwich structures under impact loadings: experimental, numerical and theoretical analysis. Thin-Walled Struct 2024;196:111541.

[27] Jeon I, Katou K, Sonoda T, Asahina T, Kang K-J. Cell wall mechanical properties of closed-cell al foam. Mech Mater 2009;41(1):60–73.

[28] Sun Y, Amirrasouli B, Razavi SB, Li Q, Lowe T, Withers P. The variation in elastic modulus throughout the compression of foam materials. Acta Mater 2016;110:161–74.

[29] Vaswani A. Attention is all you need. Adv Neural Inf Process Syst 2017.

[30] Loshchilov I, Hutter F. Decoupled weight decay regularization. 2019, arXiv:1711.05101.

[31] Odahara S, Murakami Y, Inoue M, Sueoka A. Fatigue failure by in-line flow-induced vibration and fatigue life evaluation. JSME Int J Ser A Solid Mech Mater Eng 2005;48(2):109–17.

[32] Xiao M, Wu Y, Zuo G, Fan S, Yu H, Shaikh ZA, Wen Z. Addressing overfitting problem in deep learning-based solutions for next generation data-driven networks. Wirel Commun Mob Comput 2021;2021(1):8493795.

[33] Hyndman RJ, Koehler AB. Another look at measures of forecast accuracy. Int J Forecast 2006;22(4):679–88.

[34] Ashby MF, Gibson LJ. Cellular solids: structure and properties. Press Synd Univ Camb Camb UK 1997;175–231.

[35] Wang Z-H, Lin J, Zhao L-M. Elasto-plastic constitutive model of aluminum alloy foam subjected to impact loading. Trans Nonferr Met Soc China 2011;21(3):449–54.

[36] Li S, Liu Y, Chen D, Jiang Y, Nie Z, Pan F. Encoding the atomic structure for machine learning in materials science. Wiley Interdiscip Rev: Comput Mol Sci 2022;12(1):e1558.

[37] Hangai Y, Sakaguchi Y, Kitahara Y, Takagi T, Kenji O, Yuuki T. Plateau stress estimation of aluminum foam by machine learning using X-ray computed tomography images. Int J Adv Manuf Technol 2024;132(9):5053–61.

[38] Raj RE, Daniel B. Prediction of compressive properties of closed-cell aluminum foam using artificial neural network. Comput Mater Sci 2008;43(4):767–73. http://dx.doi.org/10.1016/j.commatsci.2008.01.041, URL https://www.sciencedirect.com/science/article/pii/S0927025608000785.

[39] Sun J, Xu Y, Wang L. Evaluation of the elastic modulus and plateau stress of a 2D porous aluminum alloy based on a convolutional neural network. Metals 2023;13(2):284.

[40] Settgast C, Abendroth M, Kuna M. Constitutive modeling of plastic deformation behavior of open-cell foam structures using neural networks. Mech Mater 2019;131:1–10. http://dx.doi.org/10.1016/j.mechmat.2019.01.015, URL https://www.sciencedirect.com/science/article/pii/S0167663618306367.

[41] Islam MA, Brown AD, Hazell P, Kader M, Escobedo J, Saadatfar M, Xu S, Ruan D, Turner M. Mechanical response and dynamic deformation mechanisms of closed-cell aluminium alloy foams under dynamic loading. Int J Impact Eng 2018;114:111–22.

[42] xiang Zhu S, Ji C, geng Li R, fu Zhang Q, fei Wang P, gui Huang H. Engineering compression constitutive model of closed-cell aluminum foams at high and low temperatures. Thin-Walled Struct 2025;209:112966. http://dx.doi.org/10.1016/j.tws.2025.112966, URL https://www.sciencedirect.com/science/article/pii/S0263823125000606.

[43] Gibson L, Ashby M, Zhang J, Triantafillou T. Failure surfaces for cellular materials under multiaxial loads—I.modelling. Int J Mech Sci 1989;31(9):635–63. http://dx.doi.org/10.1016/S0020-7403(89)80001-3, URL https://www.sciencedirect.com/science/article/pii/S0020740389800013.

[44] Deshpande V, Fleck N. Isotropic constitutive models for metallic foams. J Mech Phys Solids 2000;48(6):1253–83. http://dx.doi.org/10.1016/S0022-5096(99)00082-4, URL https://www.sciencedirect.com/science/article/pii/S0022509699000824.

[45] Chen C, Lu T. A phenomenological framework of constitutive modelling for incompressible and compressible elasto-plastic solids. Int J Solids Struct 2000;37(52):7769–86. http://dx.doi.org/10.1016/S0020-7683(00)00003-2, URL https://www.sciencedirect.com/science/article/pii/S0020768300000032.

[46] Settgast C, Abendroth M, Kuna M. Constitutive modeling of plastic deformation behavior of open-cell foam structures using neural networks. Mech Mater 2019;131:1–10. http://dx.doi.org/10.1016/j.mechmat.2019.01.015, URL https://www.sciencedirect.com/science/article/pii/S0167663618306367.